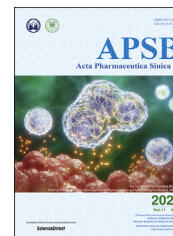




Chinese Pharmaceutical Association
Institute of Materia Medica, Chinese Academy of Medical Sciences

Acta Pharmaceutica Sinica B

www.elsevier.com/locate/apsb
www.sciencedirect.com



ORIGINAL ARTICLE

The cellular immunotherapy of integrated photothermal anti-oxidation Pd–Se nanoparticles in inhibition of the macrophage inflammatory response in rheumatoid arthritis



Chuping Zheng^a, Aiping Wu^a, Xinyun Zhai^c, Hong Ji^a,
Zhikang Chen^a, Xu Chen^{b,*}, Xiyong Yu^{a,*}

^aKey Laboratory of Molecular Target & Clinical Pharmacology and the State Key Laboratory of Respiratory Disease Pharmacological Group, School of Pharmaceutical Sciences & the Fifth Affiliated Hospital, Guangzhou Medical University, Guangzhou 511436, China

^bThe First Affiliated Hospital, Jinan University, Guangzhou 510632, China

^cNankai University, School of Materials Science & Engineering, Tianjin Key laboratory of Rare earth materials & applications, Center of Rare earth & Inorganic functional materials, Tianjin 300350, China

Received 4 November 2020; received in revised form 25 January 2021; accepted 2 February 2021

KEY WORDS

Rheumatoid arthritis;
Inflammatory response;
Photothermal therapy;
Anti-oxidation therapy;
Core–shell structure

Abstract Reducing the inflammatory response is a major goal in the therapy of rheumatoid arthritis (RA). Herein, we integrated palladium nanoparticles (Pd NPs) with selenium nanoparticles (Se NPs) and obtained a multiple nanosystem (Pd@Se-HA NPs) that could simultaneously scavenge hydroxyl radicals ($\cdot\text{OH}$) and provide a photothermal effect. The Pd@Se-HA NPs were constructed by a simple self-assembly method in which Se NPs were electrostatically bonded to Pd NPs; hyaluronic acid (HA) was linked to the NPs by ester bonding to provide macrophage targeting ability. The experiments show that the combined therapy of eliminating $\cdot\text{OH}$ with Se NPs and utilizing PTT with Pd NPs could effectively reduce the inflammatory response in macrophages more effectively than either individual NP treatment. In addition, the outer layer of HA could specifically target the CD44 receptor to enhance the accumulation of Pd@Se NPs at the lesion, further enhancing the therapeutic effect. After treatment for 15 days, the Pd@Se-HA NPs nearly eliminated the inflammatory response in the joints of mice in an induced RA model, and prevented joint damage and degradation.

*Corresponding authors.

E-mail addresses: yuxycn@aliyun.com (Xiyong Yu), chenx0816@jnu.edu.cn (Xu Chen).

Peer review under responsibility of Chinese Pharmaceutical Association and Institute of Materia Medica, Chinese Academy of Medical Sciences.

<https://doi.org/10.1016/j.apsb.2021.02.021>

2211-3835 © 2021 Chinese Pharmaceutical Association and Institute of Materia Medica, Chinese Academy of Medical Sciences. Production and hosting by Elsevier B.V. This is an open access article under the CC BY-NC-ND license (<http://creativecommons.org/licenses/by-nc-nd/4.0/>).

1. Introduction

Inflammatory responses play an important role in the initiation and development of many diseases, and numerous studies show that almost 90% of diseases have an inflammatory component^{1–5}. An excessive inflammatory response has become a factor promoting the development of many diseases, such as cancer^{4–6}, Alzheimer's disease^{7–10} and rheumatoid arthritis (RA)^{11–15}. Especially in RA, the inflammatory response can rapidly recruit immune cells to joints, including macrophages, neutrophils and T cells, and produce and secrete proinflammatory cytokines and reactive oxygen species (ROS). This results in joint swelling, joint degradation, and loss of mobility^{16–20}. In addition to proinflammatory cytokines, ROS are another damaging biological product for patients. During the inflammatory response the high concentration of ROS produced by macrophages can quickly induce chondrocyte apoptosis and eventually cause cartilage erosion. Hydroxyl radicals ($\cdot\text{OH}$) are the most common in RA patients^{16,21–23}, causing irreversible joint damage. Therefore, eliminating the generation of $\cdot\text{OH}$ to prevent the damage of articular cartilage during the inflammatory response is an urgent problem.

Selenium (Se) is an essential nutrient for humans, and selenoenzymes are vital antioxidants in the body^{24–27}. However, the activities of selenoenzymes are inhibited in inflammatory micro-environment, making it necessary to provide exogenous antioxidants^{28–30}. The development of nanotechnologies provides an effective solution to such problems^{31–35}. Selenium nanoparticles (Se NPs) have been available for many years, have good biocompatibility, and exhibit good anti-tumor activity^{36–38}. However, evidence that Se NPs directly eliminate $\cdot\text{OH}$ is not well established. According to the antioxidant mechanism of selenium compounds, Se NPs are expected to be $\cdot\text{OH}$ scavengers. However, due to the complicated pathology and mechanisms of inflammation, eliminating $\cdot\text{OH}$ will not completely eliminate tissue damage. Therefore, to better treat RA, a multiple pathway therapy is needed to suppress the inflammatory response.

Photothermal therapy (PTT) as a new treatment method has many advantages; it is non-invasive, readily controlled, and few adverse effects. PTT recently has been applied in the treatment of cancer by directly ablating the cancer cells^{39,40}. Proper hyperthermia can ablate the inflammatory cells in sites of inflammation, increase the blood circulation, promote inflammatory response dissipation and reduce the infiltration of inflammatory cells^{41,42}. Pandey et al.⁴³ also found that PTT *in vivo* can cause the dissipation of the inflammatory response and reduce the infiltration of inflammatory cells, thereby enhancing the therapeutic effect. As a photothermal reagent, palladium nanoparticles (Pd NPs) have good photothermal activity and are useful in RA therapy^{44,45}. Based on this, we combined Se NPs and Pd NPs to simultaneously eliminate the $\cdot\text{OH}$ and access PTT in RA to suppress the

macrophage inflammatory response. To effectively integrate the two nanoparticles into a system, we used the synthesis methods of core-shell structure nanoparticles. We first synthesized ultrasmall Pd NPs with positive potential, after which selenium is adsorbed onto the surface by static charge and then reduced to sodium selenite to obtain Pd@Se integrated nanoparticles. To enhance the targeting of the Pd@Se NPs we coated the NPs with hyaluronic acid (HA). The following experimental results show that the combined anti-oxidant therapy and PTT effectively inhibited the macrophage-mediated inflammation. *In vivo* Pd@Se-HA NPs effectively suppressed inflammation in arthritis and prevented the degeneration of joints, thereby effectively treating RA (Scheme 1).

2. Materials and methods

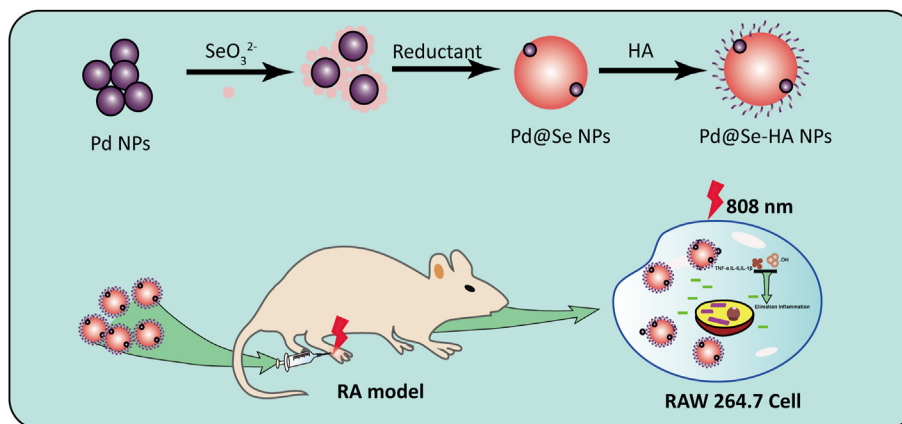
Ascorbic acid (99%), sodium tetrachloropalladate (99%), and hyaluronic acid (MW ~20 kDa) were purchased from Aladdin Chemical Shanghai Co., China. Sodium selenite (Na_2SeO_3 , 99%), lipopolysaccharides (LPS, from *Escherichia coli* O55:B5), 4-dimethylaminopyridine (DMAP) and other chemicals were purchased from Sigma-Aldrich, Beijing, China, and were reagent grade and used without further purification, unless otherwise indicated. Reagent grade water was obtained from a Milli-Q water purification system (Millipore, Bedford, USA). The RAW 264.7 cells were obtained from ATCC (Jinan University, College of Life Science and Technology, Guangzhou, China).

2.1. Synthesis of ultrasmall Pd NPs

First, 10.0 mg of sodium tetrachloropalladate was dissolved in 10.0 mL of deionized water and mixed with 150.0 mg of poly(vinylpyrrolidone) with stirring for 10 min. Ascorbic acid solution (10.0 mL, 3.0 mg/mL) was added gradually and stirred for 6 h. The solution was washed and pelleted by centrifugation three times, the supernatant was removed, and the black pellets were collected and air dried to obtain the Pd NPs powder.

2.2. Synthesis of ultrasmall Pd@Se-HA NPs

Five mg of Pd NPs powder was dissolved in 1.0 mL of deionized water and after 10 min of ultrasonication the solution was added to 10.0 mL of sodium selenite (3.0 mg/mL) and stirred for 10 min. Ascorbic acid (60.0 mg) was added to obtain Pd@Se NPs. To coat HA onto the surface of Pd@Se NPs we used esterification to conjugate HA to Pd@Se NPs, as follows: HA (2.0 g) was dissolved in anhydrous DMSO (10.0 mL) and then activated with 1-ethyl-3-(3-dimethylaminopropyl)-carbodiimide (EDC, 230.0 mg) and DMAP (5.0 mg) for 30 min under nitrogen, after which we added 2 g Pd@Se NPs and stirred for 24 h under nitrogen gas.



Scheme 1 The process of palladium (Pd) and hyaluronic acid (HA) integrated into selenium (Se) nanoparticles (Pd@Se-HA NPs) synthesis and therapy rheumatoid arthritis (RA) by combination therapy inhibiting the macrophage inflammatory response *in vivo*.

2.3. Detecting the photothermal effect of Pd@Se-HA NPs

To examine the photothermal behavior of PdNPs, Pd@Se NPs and Pd@Se-HA nanoparticles with irradiation by laser, 1 mL of the aqueous solutions of nanoparticles at different concentrations (40.0, 20.0, and 10.0 $\mu\text{g/mL}$) were aliquoted into Eppendorf tubes. The samples were irradiated by laser at 808 nm at a power density of 0.5 W/cm^2 with the exposure times from 0 to 600 s. Pre- and post-irradiated temperatures were taken by an infrared thermal imaging camera (YH-E4, FLIR, Wilsonville, USA).

2.4. Scavenging $\cdot\text{OH}$

$\text{FeSO}_4 \cdot 7\text{H}_2\text{O}$ (18 mg) was dissolved in 10 mL of deionized water (pH3–4), and 10 μL of hydrogen peroxide solution (H_2O_2 , 30%) was diluted to 10 mL. Then, 10 mL of diluted H_2O_2 was added to 10 mL of FeSO_4 solution and allowed to react for 10 min, after which the solution was aliquoted into 6-well plates (2.0 mL for each of four groups). Then 20 μL of 2.0 mg/mL Se NPs, Pd@Se NPs and Pd@Se-HA NPs were added and allowed to react for 1 h. Another group was set as a blank control group, and each group had three replicate groups. After reacting for 10 min, 0.5 mmol/L TA solution (10.0 mL in *N,N*-dimethylformamide [DMF]) was added and allowed to react for 5 min. Fluorescence intensity was measured with a fluorescence spectrophotometer (F4500, USA).

The scavenging of ($\cdot\text{OH}$) was calculated according to the following Eq. 1):

$$\text{Elimination (\%)} = [(F_0 - F) / F_0] \times 100 \quad (1)$$

where F_0 and F were the fluorescent intensities or absorbance value of a probe in the absence and presence of nanoparticles, respectively.

2.5. Cell survival detection

Cell viability of RAW 264.7 and HEK 293 T cells was measured using a colorimetric assay in 96-well plates with 2-(4-iodophenyl)-3-(4-nitrophenyl)-5-(2,4-disulfophenyl)-2H-tetrazolium monosodium salt (CCK-8) reagent. Each plate contained blanks, controls, and two dilution series with three replicates each. Cells were added to the plates at a concentration of 5×10^4 cells/mL (in DMEM/F12 with

10% FBS) and cultured for 12 h. Then different concentrations of nanoparticles (0, 50.0, 100.0 and 200.0 $\mu\text{g/mL}$) were added and incubated for another 24 h. After incubation we removed the culture medium and added 100.0 μL fresh culture medium and 10.0 μL of CCK-8 and the cells were incubated for an additional 1 h. Cell viability was measured at 450 nm in a microplate reader (Epoch2, Bio-Tek, Vermont, USA).

2.6. Detection of cellular uptake

RAW 264.7 cells (2.0 mL, 1×10^5) were inoculated into glass bottom cell culture plates (20 mm, NEST). After 6 h, 20 μL of LPS (100.0 ng/mL) was added to activate the cells. After 12 h, 20 μL of FITC-labeled Pd@Se NPs and Pd@Se-HANPs were added to a concentration of 20.0 $\mu\text{g/mL}$. After incubation for 0, 2, and 6 h they were washed three times with PBS and stained with DAPI for 15 min, and cellular fluorescence was measured by confocal laser scanning microscopy (CLSM) with the excitation wavelength at 488 nm and an emission peak at 518 nm (LSM 800, ZEISS, Oberkochen, Germany).

2.7. Detection of intracellular ROS

LPS-activated RAW264.7 cells (1×10^5) were seeded in glass bottom cell culture plates and incubated for 6 h, and then mixed with 20.0 μL of medium containing Pd NPs with/without laser, Se NPs, Pd@Se NPs with laser and Pd@Se-HA NPs with laser (20.0 $\mu\text{g/mL}$). After incubating the cells with the nanoparticles for 6 h, the cells were washed three times with PBS and stained with a ROS probe (DCFH-DA) for 30 min. After washing again in PBS, the fluorescence in cells was measured by CLSM with the excitation wavelength at 495 nm and an emission peak at 525 nm.

2.8. Anti-inflammatory response

Activated RAW 264.7 cells at a density of 1×10^5 cells per well were seeded onto 6-well plates. After culturing for 6 h, the cells were exposed to different concentrations of medium containing Pd NPs with/without laser, Se NPs, Pd@Se NPs with laser and Pd@Se-HA NPs with laser (20.0 $\mu\text{g/mL}$), and then co-incubated for another 12 h. The cells were lysed in 100.0 μL of PBS with proteinase inhibitor cocktail and cleared by centrifugation. Concentrations of

TNF- α , IL-1 β , IL-6, IL-4, IL-10 and TGF- β 1 in cell culture supernatants were measured by CBA using a mouse inflammatory kit (BD Bioscience, Franklin Lake, USA) according to the manufacturer's instructions. The cytokine analysis in joints from mice was same as carried out *in vitro*. Subsequently, typical inflammatory cytokines in the culture supernatant (TNF- α , IL-1 β , IL-6, IL-4, IL-10 and TGF- β 1) were determined by ELISA (4A Biotech, Beijing, China), while the levels of total protein were quantified by BCA (Beyotime, Shanghai, China).

2.9. Animals and animal models

Female Kunming mice were purchased from the Guangdong Medical Experimental Animal Center and animal care was in accordance with the institutional guidelines and approved by the Animal Care and Use Committee of Guangzhou Medical University, Guangzhou, China.

Briefly, 200.0 μ g bovine type II collagen emulsified in 200 μ g incomplete Freund's adjuvant (IFA) was injected into the joints at the base of the hindlimbs of mice. Ten days after the primary immunization a booster was administered subcutaneously (100 μ g bovine type II collagen emulsified in 100 μ g IFA). The progression of rheumatoid arthritis was monitored *via* scoring of each limb according to a published standard. Twenty-one days after the primary immunization, the RA mice were divided into 5 groups to receive either saline (6 mice in every group), 100 μ L Pd NPs with laser, Se NPs, Pd@Se NPs with laser or Pd@Se-HA NPs with laser, and the untreated mice served as control groups. Each sample was administered *via in situ* injections every 3 days. During the 15-day treatment period hindlimbs of RA mice were clinically scored from 0 to 4 for severity of inflammation. Briefly, synovial inflammation and cartilage erosion were evaluated as follows: 0 means no sign of inflammation, 1 means mild inflammation with minimal hyperplasia of the synovial lining layer with cartilage destruction, and 2–4 means increasing degrees of inflammatory cell infiltration or cartilage and bone destruction. The individual scores were summed to give a maximum possible score of 4 per mouse.

2.10. Histopathology evaluation

The mice were anesthetized and sacrificed at 36 days. Joints were extracted, fixed, decalcified and paraffin embedded for histopathological examination. Joint tissues were sectioned (5 μ m thick) for hematoxylin and eosin (H&E) to observe the degree of cartilage erosion. To evaluate the inflammation in joints, immunohistochemistry and immunofluorescence were used. Deparaffinized sections of joints were incubated with four specific antibodies conjugated TNF- α , IL-1 β and IL-6. The frozen sections (9 μ m) of extracted joints were fixed in 4% PFA for 30 min at 25 $^{\circ}$ C, incubated with rabbit anti-mouse TNF- α (1:500, bs-5780 R, BIOSS ANTIBODIES, Beijing, China), rat anti-mouse IL-1 β (1:500, bs-20449 R, BIOSS ANTIBODIES), or anti-mouse IL-6 (1:500, bs-6309 R, BIOSS ANTIBODIES). Then anti-rat secondary antibody (1:100, BIOSS ANTIBODIES) were added. All images were obtained by microscopy (Leica Microsystems, Wetzlar, Germany). Data were obtained from 3 to 5 non-overlapping fields per section and 3–5 sections per treatment, with 3–5 mice per treatment. All histologic studies were performed independently and assessed blindly by three trained individuals.

3. Results and discussion

3.1. Synthesis and characterization of Pd@Se-HA NPs

According to the synthesis method of core–shell structure^{40,45}, to construct the nanocomposites Pd@Se-HA NPs, we used an electrostatic reaction where SeO_3^{2-} is adsorbed around the ultra-small Pd NPs, after which reducing agents were added to reduce the SeO_3^{2-} to Se NPs on the surface of Pd NPs. Transmission electron microscopy (TEM) images showed that the Pd nanoparticles were spherical and about 5 ± 2 nm (Fig. 1A). After coating the Se NPs with HA, the Pd@Se-HA NPs were obtained with good dispensability, and the size was increased to around 125 nm (Fig. 1B). As SeO_3^{2-} can coordinately bond with Pd NPs during the process, the Pd NPs will be coated with Se NPs after to yield Pd@Se NPs. High resolution transmission electron microscopy (HR-TEM) images clearly distinguish the small nanosphere on the edge of Pd@Se-HA NPs (the red arrows) as Pd NPs since their size was similar to the size of Pd NPs (Fig. 1C). However, due to hydrogen bonds between the nanoparticles and H_2O , dynamic light scattering (DLS) yields a larger particle size than TEM (Fig. 1D)³². Under laser irradiation we found that the solutions of Pd NPs, Pd@Se NPs and Pd@Se-HA NPs produce an obvious Tyndall effect, which demonstrates that the nanoparticles are a uniform nanosol (Fig. 1E). To confirm the synthesis methods and the interaction between the components of Pd@Se-HA NPs, we first observed the absorption peak changes of the palladium source ($[\text{PdCl}_4]^{2-}$) during the synthesis of Pd NPs by UV–Vis. The results are shown in Supporting Information Fig. S1. Before adding the reducing agents to generate Pd NPs, the absorption peak of $[\text{PdCl}_4]^{2-}$ solution was at 426 nm, which is derived from the $n \rightarrow \pi^*$ electronic transition. However, after adding the reducing agents, the absorption peak at 426 nm gradually weakened, and a new absorption peak appeared at 266 nm, indicating that Pd NPs were generated. After 6 h, the adsorption peak at 426 nm disappeared, indicating that the $[\text{PdCl}_4]^{2-}$ was almost completely converted to Pd NPs. After the synthesis of Pd@Se NPs and Pd@Se-HA NPs, the absorption peak of PdNPs at 266 nm was retained, and a peak appeared at 300 nm, indicating the successful synthesis of Pd@Se-HA NPs (Fig. 1F). The absorbance and color of Pd@Se-HA NPs was concentration-dependent (Supporting Information Fig. S2). In addition, we measured the ratio of Pd and Se elements in Pd–Se NPs, with results showing that the content of Se was 88.24%, and the Pd NPs was 10.63% (Supporting Information Fig. S3). With Fourier Transform Infrared Spectrometry (FT-IR), the stretching vibration absorption peaks of –OH and –CO at 3300 and 1690 cm^{-1} further demonstrate that HA is connected to the surface of Pd@Se NPs through ester linkage (Fig. 1G).

3.2. The photothermal effect of Pd@Se-HA NPs

Although Pd NPs are good photothermal reagents when irradiated at 808 nm^{44,45}, their effectiveness when coated with Se NPs was not known. We measured the photothermal effect of 20.0 μ g/mL Pd NPs, Pd@Se NPs and Pd@Se-HA NPs irradiated with 808 nm by laser (0.5 W/cm^2) for 10 min (Fig. 2A). As expected, the Pd NPs exhibited excellent photothermal effects, with the temperature increasing rapidly during irradiation and reaching 60.1 $^{\circ}$ C. In addition, after encapsulation with Se NPs and bonding with HA, Pd@Se NPs and Pd@Se-HA NPs also showed a good photothermal effect. After laser irradiation for 10 min the temperature

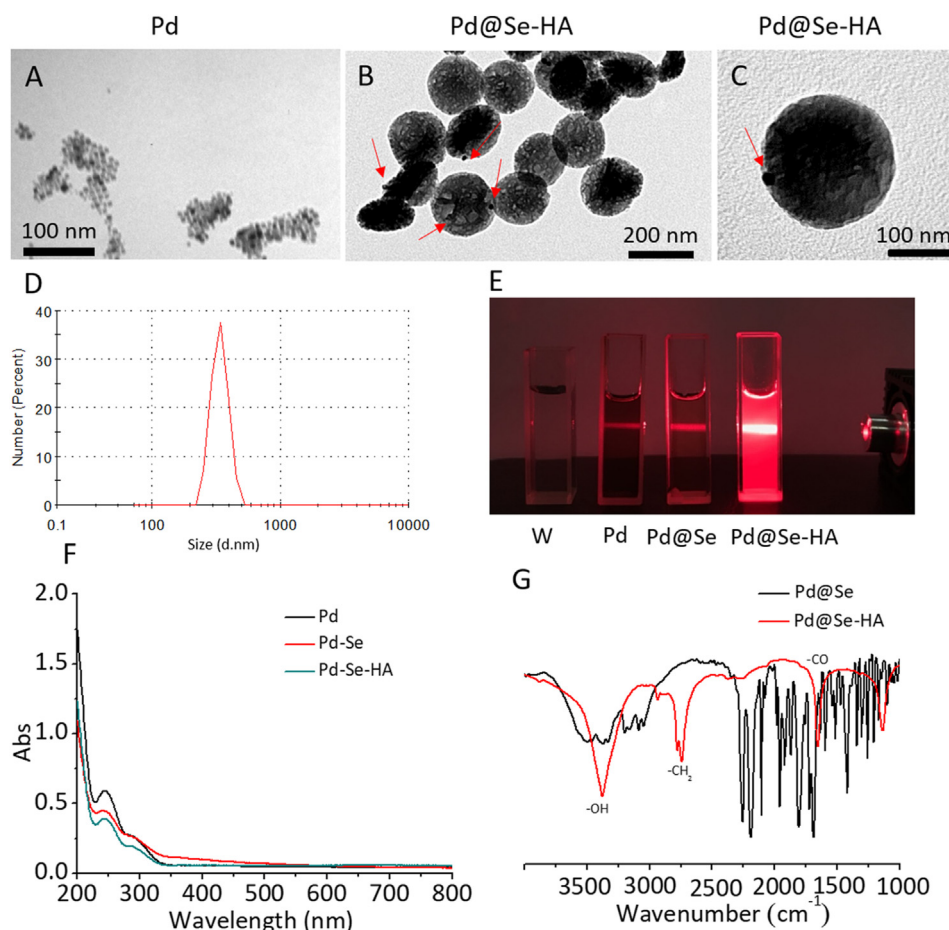


Figure 1 (A) The TEM image of Pd NPs. (B) The TEM image of Pd@Se-HA NPs. (C) The HR-TEM image of Pd@Se-HA NPs. (D) The size of Pd@Se-HA NPs detected by DLS. (E) The tintal effect of water (W), Pd NPs, Pd@Se NPs, Pd@Se-HA NPs. (F) The UV–Vis spectrum of Pd NPs, Pd@Se NPs, Pd@Se-HA NPs. (G) The FT-IR spectrum of Pd@Se NPs, Pd@Se-HA NPs.

of Pd@Se NPs and Pd@Se-HA NPs reached 47.2 and 44.5 °C, respectively. Corresponding results were obtained for the photothermal images (Fig. 2B). These results indicated that the photothermal effect of Pd@Se NPs and Pd@Se-HA NPs was lower than that of Pd NPs alone, and may be attributed to a shielding effect of Se NPs. In further testing we found that the photothermal effect of Pd@Se-HA NPs exhibits a concentration effect (Fig. 2C), with the photothermal effect gradually increasing from 10.0 to 40.0 µg/mL, and the temperature reaching 40.2, 44.5, and 50.4 °C after irradiation for 10 min, respectively (Fig. 2D). To ensure a good photothermal effect while reducing damage to normal tissues, we selected 20.0 µg/mL Pd@Se-HA NPs for subsequent treatments. Based on the cooling images (Fig. 2E) and the related linear graph (Fig. 2F) of Pd@Se-HA NPs, the photothermal conversion efficiency of Pd@Se-HA NPs was 34.5%. Therefore, based on the above experimental results, Pd@Se-HA NPs are a good photothermal agent and provide low temperature PTT for RA therapy.

3.3. The ability of Pd@Se-HA NPs to scavenge •OH

ROS is the main factor in joint loss, especially the •OH, which has the strongest activity. Reduction or elimination of •OH is an important goal for RA therapy^{6,11}. In order to measure the ability of Pd@Se-HA NPs to eliminate •OH, we used a variety of methods to

detect the concentration of •OH after treatment. TMB is a primary method for detecting •OH in solution. In the presence of •OH, TMB is easily oxidized to produce a blue substance with an absorption peak at 650 nm in UV–Vis spectrum. We tested the concentration of •OH in all the groups and the results are shown in Fig. 3A. As shown, the absorbance of TMB in the control groups and the Pd NPs groups did not change. But with the Se NPs, Pd@Se NPs and Pd@Se-HA NPs the absorbance at 650 nm was significantly decreased, indicating that Se NPs, Pd@Se NPs and Pd@Se-HA NPs could directly eliminate •OH. Compared with Pd NPs, this indicates that Se NPs play the main role in eliminating •OH. ESR assays further show that the ability of Pd@Se-HA NPs to eliminate •OH was concentration-dependent. When the concentration reached 20.0 µg/mL, the •OH were completely eliminated (Fig. 3B). Similar results were obtained with the measurement of terephthalic acid (TA). In ROS solutions TA is easily oxidized to 2-hydroxyterephthalic acid with a fluorescent peak at 425 nm. After adding various concentrations of Pd@Se-HA NPs, the intensity of the fluorescence at 425 nm was clearly decreased (Fig. 3C). After calculating the scavenging efficiency of •OH in the treated groups, we found that the •OH scavenging efficiency of Pd@Se-HA NPs was as high as 80.06% at 5.0 µg/mL, 86.1% at 10.0 µg/mL, and further improved to 91.3% and 98.6% at 20.0 and 40.0 µg/mL, respectively (Fig. 3D). The above results indicate that Pd@Se-HA NPs possess good

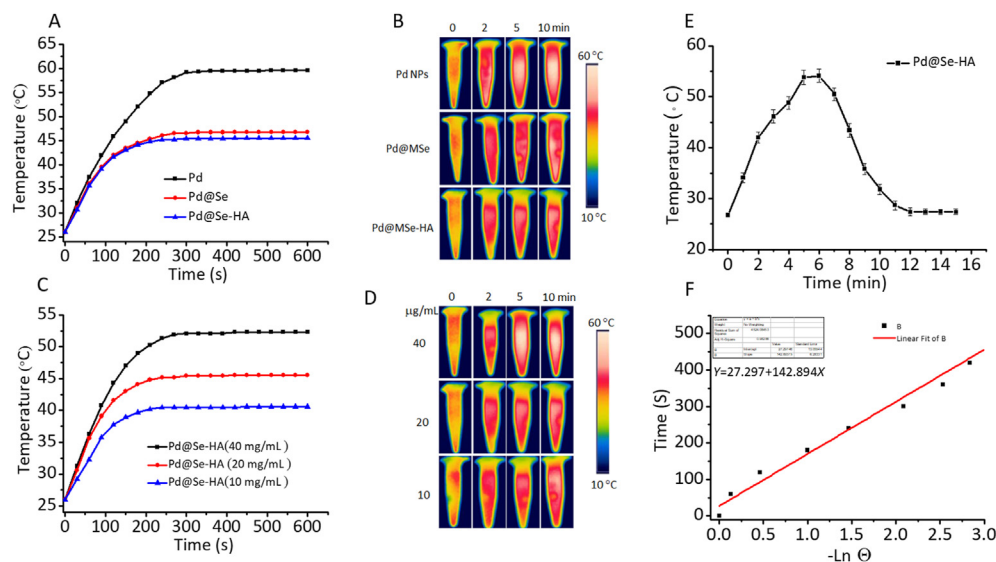


Figure 2 (A) The temperature profiles of Pd NPs (20.0 $\mu\text{g/mL}$), Pd@Se NPs (20.0 $\mu\text{g/mL}$) and Pd@Se-HA NPs (20.0 $\mu\text{g/mL}$) irradiated at 808 nm (0.5 W/cm^2) for 10 min respectively. (B) The photothermal images of Pd NPs (20.0 $\mu\text{g/mL}$), Pd@Se NPs (20.0 $\mu\text{g/mL}$) and Pd@Se-HA NPs (20.0 $\mu\text{g/mL}$). (C) The temperature profiles of different concentration Pd@Se-HA NPs (40.0, 20.0, 10.0 $\mu\text{g/mL}$) irradiated at 808 nm (0.5 W/cm^2) for 10 min respectively. (D) The photothermal images of different concentration Pd@Se-HA NPs (20.0 $\mu\text{g/mL}$) nanoparticles. (E) The monitored temperature change curves of Pd@Se-HA NPs as irradiated by the NIR laser for 600 s, followed by natural cooling with the laser light turned off, and determination of the time constant for heat transfer from the system using linear regression of the cooling profiles (mean \pm SD, $n = 3$). (F) The linear regression curves of Pd@Se-HA NPs.

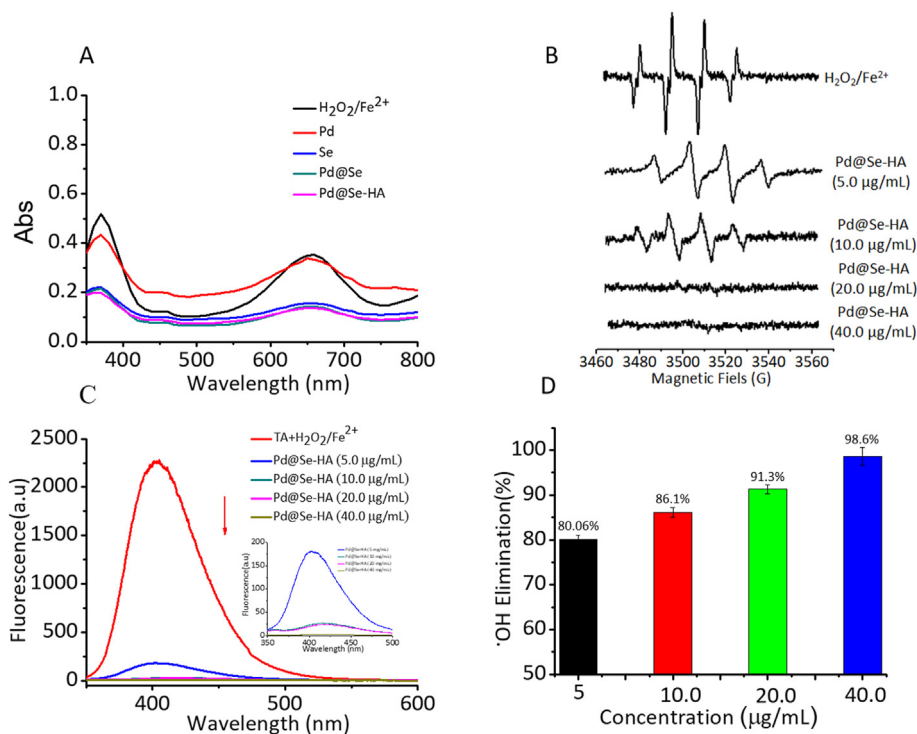


Figure 3 (A) The absorbance spectra of TMB solutions treated with $\text{Fe}^{2+}/\text{H}_2\text{O}_2$, Se NPs, Pd@Se NPs and Pd@Se-HA NPs (20 $\mu\text{g/mL}$) by microplate reader. (B) EPR spectra of $\text{Fe}^{2+}/\text{H}_2\text{O}_2$ and different concentration of Pd@Se-HA NPs respectively. (C) The fluorescent spectra of $\text{Fe}^{2+}/\text{H}_2\text{O}_2$ and different concentration of Pd@Se-HA NPs respectively. (D) The $\cdot\text{OH}$ elimination of different concentration Pd@Se-HA NPs, respectively (mean \pm SD, $n = 3$).

photothermal therapy while effectively eliminating $\cdot\text{OH}$, and therefore Pd@Se-HA NPs can provide multiple treatment approaches in RA therapy.

3.4. The stability, toxicity and targeting of Pd@Se-HA NPs

To further determine the applicability of Pd@Se-HA NPs *in vivo*, we examined the stability, toxicity and targeting effects of Pd@Se-HA NPs *in vitro*. Firstly, the size of Pd@Se-HA NPs in aqueous solution, PBS and DMEM were measured. After constant monitoring over 3 days, the size of Pd@Se-HA NPs was little changed and stability was maintained in all three solutions (Fig. 4A). CCK-8 was used to detect the toxic and adverse effects of different concentrations of Pd@Se-HA NPs and the components of Pd@Se-HA NPs on RAW 264.7 and HEK 293 T cells. The results show that Pd NPs, Se NPs, and Pd@Se NPs and Pd@Se-HA NPs exhibited negligible toxicity to RAW 264.7 cells, even at a concentration of up to 200.0 $\mu\text{g}/\text{mL}$, and the survival rates of RAW 264.7 were all above 90% (Fig. 4B). HEK 293 T demonstrated similar results (Fig. 4C), which indicated that Pd@Se-HA NPs have negligible toxicity to normal cells and have no stimulating effect on immune cells. Hemolysis experiments indicate that the different concentration of Se NPs and Pd@Se-HA NPs have no unwanted effects on red blood cells. With high concentrations of Pd@Se-HA NPs there were still no changes in the osmotic pressure of red blood cells and no hemolysis (Fig. 4D). Therefore, based on the above results, we conclude that Pd@Se-HA NPs have minimal toxic side effects *in vitro*, and are suitable for cell experiments and *in vivo* studies. HA could specifically bind the CD44 receptor to activate RAW 264.7 cells^{1,4}. Therefore, to enhance the uptake of Pd@Se NPs by macrophages, we used HA molecules to attach to the surface of Pd@Se NPs. The results show that the cell uptake of Pd@Se NPs and Pd@Se-HA NPs was not different at 0 h, but after incubation for 2 h, there was a clear difference between the Pd@Se NPs and Pd@Se-HA NPs. The fluorescent intensity of Pd@Se-HA NPs is

more greatly enhanced than that of Pd@Se NPs in RAW 264.7 cells; the trend continued through 6 h (Fig. 4E). In addition, if the cells were pre-treated with HA for 2 h and Pd@Se-HA NPs were then added, the uptake decreased. This demonstrates that HA can indeed enhance the targeting of nanoparticles and increase the uptake of nanoparticles into cells.

3.5. The activity of Pd@Se-HA NPs in scavenging intracellular inflammatory response mediators and ROS

We tested the ability of Pd@Se-HA NPs to inhibit inflammation and promote ROS scavenging activity in RAW264.7 cells. To quantify the inflammatory response in RAW 264.7 cells, we used ELISA to measure the changes in pro-inflammatory cytokines (TNF- α , IL-1 β , IL-6) and anti-inflammatory cytokines (IL-4, IL-10, and TGF- β 1). The results show that Pd NPs alone had no effect on pro-inflammatory cytokine and anti-inflammatory cytokine levels, but after laser irradiation, Pd NPs effectively reduced the expression of pro-inflammatory cytokines through a photothermal effect (Fig. 5A–C), but did not promote the expression of anti-inflammatory cytokines. This demonstrates that PTT can inhibit macrophage inflammation by reducing the expression of pro-inflammatory cytokines. In addition, after treatment with Se NPs, results showed the Se NPs not only effectively inhibited the expression of pro-inflammatory cytokines, but also promoted the expression of anti-inflammatory cytokines (IL-4 and IL-10, Fig. 5D–E). This increased expression of anti-inflammatory cytokines may result from a decrease in ROS species. We expected that after adding an equal concentration of Pd@Se NPs and irradiating with laser, there would be a better anti-inflammatory effect with the combined effect of Pd NPs and Se NPs. Similarly, after linking the targeting molecule HA, the accumulation of Pd@Se NPs in RAW 264.7 cells would be enhanced. Therefore, the expression of pro-inflammatory cytokines was almost completely inhibited after treatment with Pd@Se-HA NPs for 24 h. It was interesting that all the nanoparticles can effectively inhibit the pro-inflammatory

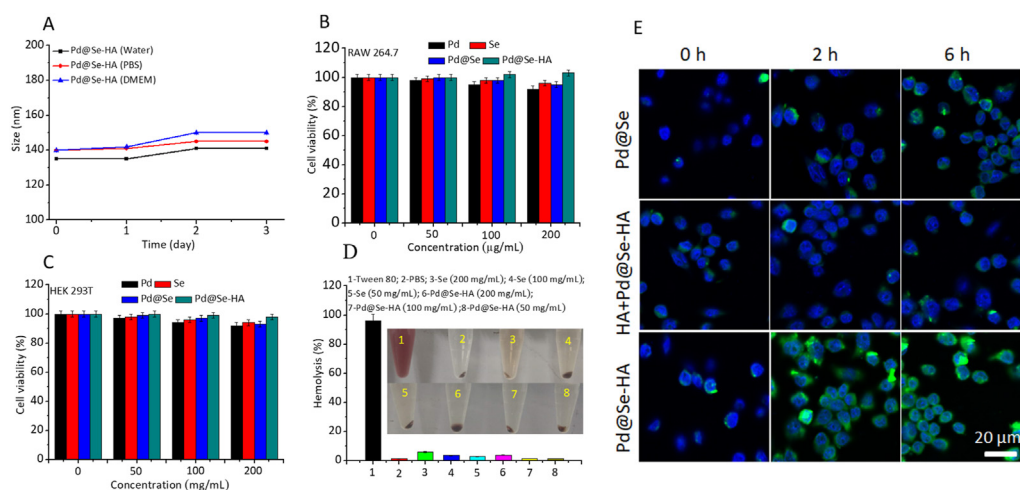


Figure 4 (A) The size stability of Pd@Se-HA NPs for 3 Days dispersed in water, PBS and DMEM respectively. (B) Relative viabilities of RAW 264.7 cells after being exposed to Pd NPs, Se NPs, Pd@Se NPs and Pd@Se-HA NPs at different concentrations for 24 h. (C) Relative viabilities of HEK 293 T cells after being exposed to Pd NPs, Se NPs, Pd@Se NPs and Pd@Se-HA NPs at different concentrations for 24 h. (D) Hemolytic activity of Se NPs and Pd@Se-HA NPs with erythrocyte stock in a Tris buffer solution (mean \pm SD, $n = 3$, $*P \leq 0.05$, $**P \leq 0.01$). (E) The uptake of Pd@Se NPs and Pd@Se-HA NPs or pre-treated with HA for 2 h than added Pd@Se-HA NPs labeled with FITC in RAW 264.7 cells at different times (0, 2, and 6 h) by CLSM, scale bar = 20 μm .

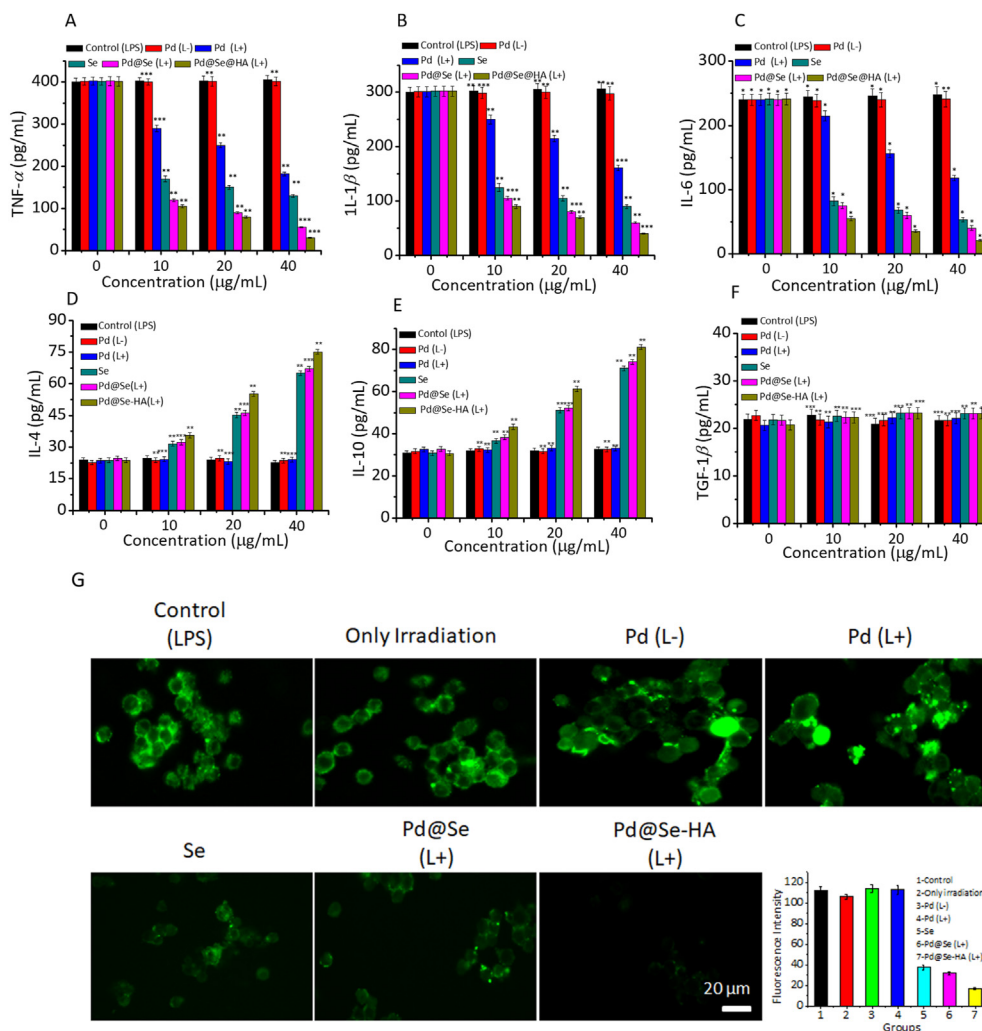


Figure 5 (A)–(C) The effects of various nanoparticles and their influence on RAW 264.7 cells associated pro-inflammatory cytokines (TNF- α , IL-1 β , IL-6) respectively. (D)–(F) The effects of various nanoparticles and their influence on RAW 264.7 cells associated anti-inflammatory cytokines (IL-4, IL-10, TGF- β 1) respectively at different concentrations for 24 h. (G) The fluorescent microscope images of ROS in RAW 264.7 cells treated with LPS (100 ng/mL) and treated with various nanoparticles for 24 h by DCFH-DA probe, respectively (mean \pm SD, $n = 3$, * $P \leq 0.05$, ** $P \leq 0.01$), scale bar = 20 μ m.

cytokines and increased the expression of anti-inflammatory factors IL-4 and IL-10, but the effect of promoting TGF- β 1 was not seen (Fig. 5F).

After measuring the expression of inflammatory cytokines, we also measured intracellular ROS levels. From the fluorescent images of the ROS probe, with comparison to untreated activated RAW 264.7 cells, only the groups of Pd NPs with/without irradiation showed strong green fluorescence and with similar fluorescence intensity after quantitative analysis. However, after incubating with Se NPs, the intracellular ROS decreased which is consistent with our earlier results, further indicating that Se NPs can directly eliminate intracellular ROS. The Pd@Se NPs and Pd@Se-HA NPs also showed similar results, indicating that the Se NPs were the main components of Pd@Se NPs for elimination of ROS. Therefore, the ROS-eliminating activity of Pd@Se NPs was similar to Se NPs, but with the better targeting ability of Pd@Se-HA NPs the generation of ROS in RAW264.7 cells was almost entirely eliminated (Fig. 5G). Based on the above results, it is evident that with the combination of PTT and Se NPs, Pd@Se-HA NPs can effectively inhibit the inflammatory response of activated

RAW 264.7 cells and greatly reduce ROS. In previous studies it was reported that PTT inhibited inflammation by destroying inflammatory cells. To further verify the mechanism of Pd@Se-HA NPs in eliminating inflammation, we determined the cell viability of RAW 264.7 cells treated with Pd@Se-HA NPs with irradiation. As shown in Supporting Information Fig. S4A, under NIR laser irradiation, the inhibitory effect of Pd@Se-HA NPs on LPS-activated RAW 264.7 cells was significant and concentration-dependent. This indicated that the Pd@Se-HA NPs under laser irradiation can inhibit the inflammatory response in RAW 264.7 cells, but Pd@Se-HA NPs have no effect on normal RAW 264.7 cells. In addition, as evident from Fig. S4B, Pd NPs, Pd@Se NPs and Pd@Se-HA NPs showed the inhibitory effect only under irradiation. These results indicate that PTT inhibited inflammation by elimination of inflammatory cells.

3.6. The effect of Pd@Se-HA NPs on RA therapy

In cell experiments, Pd@Se-HA NPs exhibited good anti-inflammatory activity. We further measured the effect of the

above-mentioned nanoparticles in the therapy of RA in mice. Firstly, we injected bovine type II collagen into the hind limb joints to induce RA. After three injections over 10 days, the RA model was successfully induced^{42,43}. Subsequently, the nanoparticles were injected through the tail vein. During the treatment period, the inflammation index was measured to indicate the severity of inflammation in each group. The inflammation index was graded 1–4 to reflect the degree of inflammation in the joints, with the higher number indicating the higher severity of inflammation. After continuous monitoring for 15 days, the inflammation was greatest in the control group, with an inflammation index of 4. After treatment with PTT and Pd NPs, the inflammation index decreased. The Se NPs showed a better effect due to the strong ability to decrease ROS and thereby inhibit the inflammatory response, and after 15 days of treatment the inflammation index decreased significantly. Pd@Se NPs and Pd@Se-HA NPs combined with PTT and anti-oxidants showed stronger ability to

reduce inflammation (Fig. 6A). We then measured pro-inflammatory cytokines in this arthritis model by ELISA. The results show the same trend with three pro-inflammatory cytokines (TNF- α , IL-6 and IL-1 β) (Fig. 6B–D), indicating that Pd@Se-HA NPs also have good anti-inflammatory effects *in vivo*. After treatment, to further demonstrate the treatment effect of Pd@Se-HA NPs, we evaluated monocyte cell infiltration and cartilage erosion by histopathology. CD86 immunofluorescence results showed that Pd@Se-HA NPs effectively inhibit the infiltration of monocytes and prevent the further development of an inflammatory response. Subsequently, we used H&E sections to monitor inflammatory cell infiltration and cartilage erosion. As shown in Fig. 6E, the joint cavity in the untreated group was infiltrated with many inflammatory cells (red arrow), and the articular cartilage was severely eroded and degraded with the continuous inflammatory response. However, after Pd@Se-HA NPs treatments the infiltration of inflammatory cells and cartilage erosion was

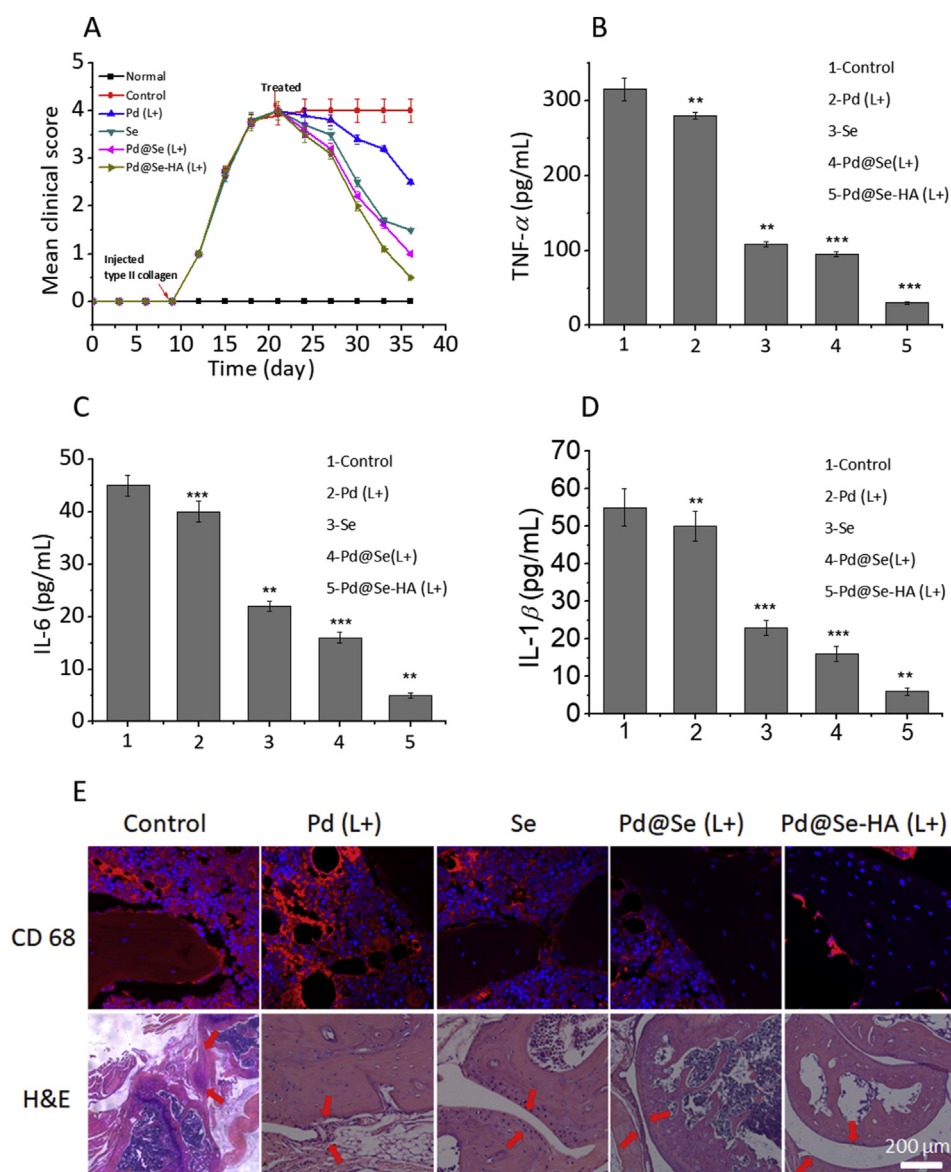


Figure 6 (A) Mean clinical score measurements for various nanoparticle treated groups during treatment over the time period. (B)–(D) Semiquantitative analysis of TNF- α , IL-6 and IL-1 β in RA mice. (E) CD 68 and H&E images of cartilage changes after treatment with each nanoparticle *in vivo* (mean \pm SD, $n = 5$, * $P \leq 0.05$, ** $P \leq 0.01$). Images were acquired at 40 \times magnification, scale bar = 200 μ m.

significantly inhibited, especially after treatment with Pd@Se-HA NPs, which completely prevented the infiltration of inflammatory cells and the erosion and degradation of cartilage. Therefore, the Pd@Se-HA NPs with the combination therapy appear to be very good agents for RA therapy.

4. Conclusions

In this study, we have constructed a nanosystem (Pd@Se-HA NPs) that combines PTT and antioxidant therapy. To integrate the Se NPs and Pd NPs into a nanosystem, we used the method of core-shell structure to embed Pd NPs (which show a photothermal effect) into Se NPs, and then bond HA molecules, which provide a targeting function, onto the surface to form Pd@Se-HA NPs with a core-shell structure. *In vitro* experiments, Pd@Se-HA NPs exhibited a good photothermal effect and $\cdot\text{OH}$ scavenging ability, and with the combined effect of Pd NPs and Se NPs, Pd@Se-HA NPs effectively inhibited macrophage infiltration, ROS production, and cytokine-mediated inflammation. The targeted action of HA further enhanced the ability of Pd@Se-HA NPs to eliminate inflammation in cells and *in vivo*. After Pd@Se-HA NPs treatment, these Pd@Se NPs effectively eliminated joint inflammation and protected joint cartilage.

Acknowledgments

This work was supported by the National Natural Science Foundation of China (No. U1601227), the Natural Science Foundation of Guangdong Province (2018A0303130139, China), the Fundamental Research Funds for the Central Universities, Nankai University (63201071, China), and the Guangzhou Educational Science Planning Foundation (201811666, China).

Author contributions

Chuping Zheng designed the research and wrote the manuscript. Xu Chen designed the research, carried out the experiments and performed data analysis. Aiping Wu and Xinyun Zhai assisted with the experiments. Hong Ji provided experimental drugs and quality control. Xiyong Yu was responsible for supervising the research and revised the manuscript. All of the authors have read and approved the final manuscript.

Conflicts of interest

The authors have no conflicts of interest to declare.

Appendix A. Supporting information

Supporting to this article can be found online at <https://doi.org/10.1016/j.apsb.2021.02.021>.

References

- Henson PM. Dampening inflammation. *Nat Immunol* 2005;**6**:1179–81.
- Hotamisligil GS. Inflammation, metaflammation and immunometabolic disorders. *Nature* 2017;**542**:177–85.
- Weinlich R, Oberst A, Beere HM, Green DR. Necroptosis in development, inflammation and disease. *Nat Rev Mol Cell Biol* 2017;**18**:127–36.
- Candido J, Hagemann T. Cancer-related inflammation. *J Clin Immunol* 2013;**33**:79–84.
- Frangogiannis NG. Inflammation in cardiac injury, repair and regeneration. *Curr Opin Cardiol* 2015;**30**:240–5.
- Munn LL. Cancer and inflammation. *Wiley Interdiscip Rev Syst Biol Med* 2017;**9**:e1370.
- Jha MK, Lee WH, Suk K. Functional polarization of neuroglia: implications in neuroinflammation and neurological disorders. *Biochem Pharmacol* 2016;**103**:1–16.
- Lampron A, ElAli A, Rivest S. Innate immunity in the CNS: redefining the relationship between the CNS and its environment. *Neuron* 2013;**78**:214–32.
- Cherry JD, Olschowka JA, O'Banion MK. Neuroinflammation and M2 microglia: the good, the bad, and the inflamed. *J Neuroinflammation* 2014;**11**:98.
- Sun J, Wei CF, Liu YN, Xie WJ, Xu MM, Zhou H, Liu J. Progressive release of mesoporous nano-selenium delivery system for the multi-channel synergistic treatment of Alzheimer's disease. *Biomaterials* 2019;**197**:417–31.
- Liu YN, Ma LT, Zhou H, Zhu XF, Yu QQ, Chen X, Zhao YY, Liu J. Polypeptide nano-Se targeting inflammation and theranostic rheumatoid arthritis by anti-angiogenic and NO activating AMPK α signaling pathway. *J Mater Chem B* 2018;**6**:3497–514.
- Chen X, Zhu XF, Xu TY, Xu MM, Wen YY, Liu YN, Liu J, Qin XY. Targeted hexagonal Pd nanosheet combination therapy for rheumatoid arthritis via the photothermal controlled release of MTX. *J Mater Chem B* 2019;**7**:112–22.
- Chen X, Liu YN, Wen YY, Yu QQ, Liu JW, Zhao YY, Liu J, Ye G. A photothermal-triggered nitric oxide nanogenerator combined with siRNA for precise therapy of osteoarthritis by suppressing macrophage inflammation. *Nanoscale* 2019;**11**:6693–709.
- Bizzaro N, Mazzanti G, Tonutti E, Villalta D, Tozzoli R. Diagnostic accuracy of the anti-citrulline antibody assay for rheumatoid arthritis. *Clin Chem* 2001;**47**:1089–93.
- Ai RZ, Laragione T, Hammaker D, Boyle DL, Wildberg A, Maeshima K. Comprehensive epigenetic landscape of rheumatoid arthritis fibroblast-like synoviocytes. *Nat Commun* 2018;**9**:1921.
- Phull AR, Nasir B, ulHaq I, Kim SJ. Oxidative stress, consequences and ROS mediated cellular signaling in rheumatoid arthritis. *Chem Biol Interact* 2017;**281**:121–36.
- Dai L, Zhang Z, Winyard PG, Gaffney K, Jones H, Blake DR. A modified form of low-density lipoprotein with increased electronegative charge is present in rheumatoid arthritis synovial fluid. *Free Radic Biol Med* 1997;**22**:705–10.
- Yang Z, Fujii H, Mohan SV, Goronzy JJ, Weyand CM. Phosphofruktokinase deficiency impairs ATP generation, autophagy, and redox balance in rheumatoid arthritis T cells. *J Exp Med* 2013;**210**:2119–34.
- Khojah HM, Ahmed S, Abdel-Rahman MS, Hamza AB, et al. Reactive oxygen and nitrogen species in patients with rheumatoid arthritis as potential biomarkers for disease activity and the role of antioxidants. *Free Radic Biol Med* 2016;**97**:285–91.
- Shang CH, Zhang QQ, Zhou JH. Oridonin inhibits cell proliferation and induces apoptosis in rheumatoid arthritis fibroblast-like synoviocytes. *Inflam* 2016;**39**:873–80.
- Basta F, Irace R, Borgia A, Messiniti V, Riccardi A, Valentini G, et al. Hydroxychloroquine significantly reduces serum markers of endothelial injury and NEMO video capillaroscopy score in systemic sclerosis. *Rheum* 2019;**58**:1303–5.
- Yu LL, Zhang WF, Huang CH, Liang Q, Bao HH, Gong ZJ, et al. FoxO₄ promotes myocardial ischemia-reperfusion injury: the role of oxidative stress-induced apoptosis. *Am J Transl Res* 2018;**10**:2890–900.
- Yang S, Chen XP, Li SL, Sun B, Hang CH. Melatonin treatment regulates SIRT3 expression in early brain injury (EBI) due to reactive oxygen species (ROS) in a mouse model of subarachnoid hemorrhage (SAH). *Med Sci Mon Int Med J Exp Clin Res* 2018;**24**:3804–14.

24. Skalickova S, Milosavljevic V, Cihalova K, Horky P, Richtera L, Adam V. Selenium nanoparticles as a nutritional supplement. *Nutrition* 2017;**33**:83–90.
25. Hosnedlova B, Kepinska M, Skalickova S, Fernandez C, Ruttkay-Nedecky B, Peng QM, et al. Nano-selenium and its nanomedicine applications: a critical review. *Int J Nanomed* 2018;**13**:2107–28.
26. Battin EE, Brumaghim JL. Antioxidant activity of sulfur and selenium: a review of reactive oxygen species scavenging, glutathione peroxidase, and metal-binding antioxidant mechanisms. *Cell Biochem Biophys* 2009;**55**:1–23.
27. Circu ML, Aw TY. Reactive oxygen species, cellular redox systems, and apoptosis. *Free Radic Biol Med* 2010;**48**:749–62.
28. Gao XY, Zhang JS, Zhang L. Hollow sphere selenium nanoparticles: their *in-vitro* anti hydroxyl radical effect. *Adv Mater* 2002;**14**:290–3.
29. Yin T, Yang L, Liu Y, et al. Sialic acid (SA)-modified selenium nanoparticles coated with a high blood–brain barrier permeability peptide-B6 peptide for potential use in Alzheimer's disease. *Acta Biomater* 2015;**25**:172–83.
30. Ruan CP, Liu CJ, Hu HL, Guo XL, Jiang BP, Liang H, et al. NIR-II light-modulated thermosensitive hydrogel for light-triggered cisplatin release and repeatable chemo-photothermal therapy. *Chem Sci* 2019;**10**:4699–706.
31. Huang CC, Chia WT, Chung MF, Lin KJ, Hsiao CW, Jin C, et al. An implantable depot that can generate oxygen *in situ* for overcoming hypoxia-induced resistance to anticancer drugs in chemotherapy. *J Am Chem Soc* 2016;**138**:5222–5.
32. Chen GJ, Xu M, Zhao S, Sun J, Yu QQ, Liu J. Pompon-like RuNPS-based theranostic nanocarrier system with stable photoacoustic imaging characteristic for accurate tumor detection and efficient phototherapy guidance. *ACS Appl Mater Interfaces* 2017;**9**:33645–59.
33. Zhang DY, Zheng Y, Zhang H, He L, Tan CP, Sun JH, et al. Ruthenium complex-modified carbon nanodots for lysosome-targeted one- and two-photon imaging and photodynamic therapy. *Nanoscale* 2017;**9**:18966–76.
34. Huang N, Chen X, Zhu XF, Xu MM, Liu J. Ruthenium complexes/polypeptide self-assembled nanoparticles for identification of bacterial infection and targeted antibacterial research. *Biomaterials* 2017;**141**:296–313.
35. Guo HH, Feng CL, Zhang WX, Luo ZG, Zhang HJ, Zhang TT, et al. Liver-target nanotechnology facilitates berberine to ameliorate cardio-metabolic diseases. *Nat Commun* 2019;**10**:1981.
36. Huang YY, Liu Z, Liu CQ, Zhang Y, Ren JS, Qu XG. Selenium-based nanozyme as biomimetic antioxidant machinery. *Chem-A Euro J* 2018;**24**:10224–30.
37. Malhotra S, Welling MN, Mantri SB, Desai K. *In vitro* and *in vivo* antioxidant, cytotoxic, and anti-chronic inflammatory arthritic effect of selenium nanoparticles. *J Biomed Mater Res B Appl Biomater* 2015;**104**:993–1003.
38. Zhai XN, Zhang CY, Zhao GH, Stoll S, Ren FZ, Leng XJ. Antioxidant capacities of the selenium nanoparticles stabilized by chitosan. *J Nanobiotechnol* 2017;**15**:4.
39. Su JH, Sun HP, Meng QS, Yin Q, Zhang PC, Zhang ZW, et al. Bio-inspired nanoparticles with NIR-controlled drug release for synergistic chemophotothermal therapy of metastatic breast cancer. *Adv Funct Mater* 2016;**26**:7495–506.
40. Chen M, Guo ZD, Chen QH, Wei JP, Li JC, Shi CR, et al. Pd nanosheets with their surface coordinated by radioactive iodide as a high-performance theranostic nanoagent for orthotopic hepatocellular carcinoma imaging and cancer therapy. *Chem Sci* 2018;**9**:4268–74.
41. Lu Y, Li LH, Lin ZF, Wang LP, Lin LJ, Li M, et al. A new treatment modality for rheumatoid arthritis: combined photothermal and photodynamic therapy using Cu_{7.2}S₄ nanoparticles. *Adv Healthcare Mater* 2018;**7**: 1800013.
42. Chen X, Zhu XF, Ma LT, Lin AG, Gong YC, Yuan GL, et al. A core–shell structure QRu-PLGA-RES-DS nanocomposite with photothermal response-induced M2 macrophage polarization for rheumatoid arthritis therapy. *Nanoscale* 2019;**11**:18209–23.
43. Pandey PK, Maheshwari R, Raval N, Gondaliya P, Kalia K, Tekade RK. Nanogold-core multifunctional dendrimer for pulsatile chemo-photothermal- and photodynamic- therapy of rheumatoid arthritis. *J Colloid Interface Sci* 2019;**544**:61–77.
44. Chen M, Tang SH, Guo ZD, Wang XY, Mo SG, Huang XQ, et al. Core–shell Pd@Au nanoplates as theranostic agents for *in-vivo* photoacoustic imaging, CT imaging, and photothermal therapy. *Adv Mater* 2014;**26**:8210–6.
45. Shi SG, Chen XL, Wei JP, Huang YZ, Weng J, Zheng NF. Platinum (IV) prodrug conjugated Pd@Au nanoplates for chemotherapy and photothermal therapy. *Nanoscale* 2016;**8**:5706–13.